

Strain induced power enhancement of far-UVC LEDs on high temperature annealed AlN templates

Cite as: Appl. Phys. Lett. **122**, 011102 (2023); doi: [10.1063/5.0134253](https://doi.org/10.1063/5.0134253)

Submitted: 9 November 2022 · Accepted: 17 December 2022 ·

Published Online: 5 January 2023



View Online



Export Citation



CrossMark

A. Knauer,^{1,a)}  T. Kolbe,¹  S. Hagedorn,¹  J. Hoepfner,²  M. Guttman,¹  H. K. Cho,¹  J. Rass,¹ 
J. Ruschel,¹  S. Einfeldt,¹  M. Kneissl,^{1,2}  and M. Weyers¹ 

AFFILIATIONS

¹Ferdinand-Braun-Institut (FBH), Gustav-Kirchhoff-Str. 4, 12489 Berlin, Germany

²Institute of Solid State Physics, Technische Universität Berlin, Hardenbergstraße 36, 10623 Berlin, Germany

Note: This paper is part of the APL Special Collection on UV/DUV Light Emitters.

^{a)}Author to whom correspondence should be addressed: arne.knauer@fbh-berlin.de

ABSTRACT

High temperature annealed AlN/sapphire templates exhibit a reduced in-plane lattice constant compared to conventional non-annealed AlN/sapphire grown by metalorganic vapor phase epitaxy (MOVPE). This leads to additional lattice mismatch between the template and the AlGaIn-based ultraviolet-C light emitting diode (UVC LED) heterostructure grown on these templates. This mismatch introduces additional compressive strain in AlGaIn quantum wells resulting in enhanced transverse electric polarization of the quantum well emission at wavelengths below 235 nm compared to layer structures deposited on conventional MOVPE-grown AlN templates, which exhibit mainly transverse magnetic polarized emission. In addition, high temperature annealed AlN/sapphire templates also feature reduced defect densities leading to reduced non-radiative recombination. Based on these two factors, i.e., better outcoupling efficiency of the transverse electric polarized light and an enhanced internal quantum efficiency, the performance characteristic of far-UVC LEDs emitting at 231 nm was further improved with a cw optical output power of 3.5 mW at 150 mA.

© 2023 Author(s). All article content, except where otherwise noted, is licensed under a Creative Commons Attribution (CC BY) license (<http://creativecommons.org/licenses/by/4.0/>). <https://doi.org/10.1063/5.0134253>

AlGaIn-based far ultraviolet-C light emitting diodes (far-UVC LEDs) with emission wavelength between 210 and 240 nm are of particular interest for sensing and *in vivo* disinfection since the short wavelength can inactivate micro-organisms without damaging the human skin or eye.^{1–6} In contrast to near-UVC-LEDs emitting at 265–280 nm, far-UVC light is germicidal and **can be used in a manned environment as well.**⁷

Unfortunately, the light output power and efficiency strongly decrease for shorter emission wavelength of AlGaIn-based LEDs.^{8–10} This is due to a reduction in the internal quantum efficiency (IQE), charge carrier injection efficiency (CIE), and light extraction efficiency (LEE) of the LEDs. Previous studies have shown a change in the dominant optical polarization from transverse electric (TE) to transverse magnetic (TM) with increasing aluminum content in the active region as well as with decreasing aluminum content offset between a quantum well (QW) and a quantum barrier (QB).^{11–17} The wavelength, at which the TM polarized light emission becomes dominant, depends

on the strain in the QW and, thus, on the stress distribution stemming from lattice mismatch between the epitaxial layers in the active region¹⁵ to the underlying AlN template^{11,17} and n-AlGaIn contact layer.¹⁸ The crossover between TE and TM was observed for emission wavelengths around 240 nm.^{12,13,16,17} As TM polarized light propagates in the in-plane direction, the light extraction efficiency from far-UVC LEDs is severely reduced. The strain-induced piezoelectric polarization can reduce the effect of the spontaneous polarization^{17–19} and, hence, influences the polarization-induced electrical fields in the QWs and their effect on the IQE.²⁰ The enhancement of TE polarization of the QW emission of far-UVC LEDs by the use of AlN/sapphire templates in comparison to bulk AlN substrates as a result of increased compressive internal strain applied to the MQWs was already demonstrated in Refs. 11 and 17. It was found that next to composition, strain has the largest influence on the degree of polarization (DOP) while all other factors were practically insignificant.¹⁷ Thus, in addition to the design of the epitaxial layers in the active region, the strain introduced

by the AlN template can also have an impact on the LEE and the output power and efficiency of far-UVC LEDs.

Currently, the reported output powers for far-UVC LEDs are poor and often measured under pulsed operation, e.g., 0.15 mW at 227 nm emission wavelength²¹ and recently 1.4 mW at 228 nm and 150 mA.²² For LEDs grown on a bulk AlN substrate, an output power of 0.225 mW for an emission wavelength of 226 nm was demonstrated²³ as well as 1.2 mW for emission near 230 nm, both under continuous wave (cw) operation.¹⁰ For LEDs on patterned sapphire substrates, output power levels of 1.9 mW have been reached at 233 nm and 100 mA (cw).²⁴

In this paper, we have investigated the effect of different AlN/sapphire templates on the DOP and the optical output power of far-UVC LEDs emitting in the range of 229–234 nm. **We will show how the increased lattice mismatch of high temperature annealed AlN/sapphire templates in comparison to MOVPE-grown AlN templates can increase the DOP and move the switching point from dominant TE to dominant TM polarized light from 245 nm on AlN bulk substrates¹⁷ or 239 nm on patterned AlN/sapphire templates^{11,16} to emission wavelengths below 230 nm. Milliwatt-power operation in cw operation could be demonstrated for LEDs emitting at 231 nm.**

The LED heterostructures were grown by metalorganic vapor phase epitaxy (MOVPE) with standard precursors on two-inch diameter (0001) oriented sapphire substrates in a close coupled shower head reactor (six times two-inch configuration). The reactor is equipped with an *in situ* control tool EpiCurveTT[®], measuring curvature, pocket temperature, and reflectivity at different wavelengths.

Three kinds of AlN/sapphire templates were used. One comprises a 2 μm thick MOVPE grown AlN layer (MOVPE-AlN), and the second one was produced by applying a double AlN deposition/growth and double annealing process (DGA-AlN) similar to the procedure described by Wang *et al.*²⁵ For this, a 0.4 μm thick AlN layer was sputtered and then annealed at 1720 °C for 3 h. Afterwards, a 1.1 μm thick AlN layer was deposited by MOVPE, and the layer stack was again annealed for 5 h at 1720 °C in N₂.^{26,27} The full widths at half maximum (FWHM) of omega rocking curves (XRCs) were determined by x-ray diffraction using Philips X'Pert Pro with a fourfold 220Ge monochromator and 0.5 mm \times 5 mm aperture on the source side and a 1° receiving slit in front of the detector. For both kinds of templates, the 00.2 FWHM was 70 arc sec. The FWHM of the 10.2 reflection was 400 arc sec in the case of MOVPE-AlN and 180 arc sec for DGA-AlN. These FWHMs correlate with a screw dislocation density of about 10⁷ cm⁻² for both kinds of templates, while the total threading dislocation densities (TDDs) are estimated to be 2 \times 10⁹ cm⁻² and 4 \times 10⁸ cm⁻² for the non-annealed MOVPE-AlN template and the DGA-AlN template, respectively.²⁸ Since the annealing processes reduce the TDD to a level of 4 \times 10⁸ cm⁻² but also decrease the AlN a-lattice constant,^{26,27,29} one DGA-AlN template was additionally overgrown by MOVPE with a 3 μm thick AlN:Si layer (AlN:Si/DGA-AlN) with a silicon concentration of about 1 \times 10¹⁹ cm⁻³ as the third template variant. The silicon doping introduces a tensile strain component by introducing vacancies, which bend preexisting dislocations. Hence, the in-plane lattice constant increases in AlN:Si with increasing layer thickness, which reduces the lattice mismatch between the MOVPE-grown AlN buffer and the underlying DGA-AlN template.^{30–33} During AlN:Si growth, the TDD remained unchanged, which was also confirmed by the XRC FWHMs of the AlN:Si/DGA-AlN template

(FWHM 00.2: 121 arc sec, 10.2: 180 arc sec) and measurement of the dark spot density by laterally resolved cathodoluminescence (CL). The Al mol fraction (x), the degree of relaxation, and the lattice constants were confirmed by x-ray diffraction reciprocal space maps in 00.4 and 11.4 reflection using a Panalytical X'Pert³ system with a PIXcel array detector. The accuracy of the Al content x is \pm 0.005, and the accuracy of the relaxation degree is about 5% points. The AlN a-lattice constants of the three different AlN templates were determined as $a(\text{DGA-AlN}) = 3.100$, $a(\text{AlN:Si/DGA-AlN}) = 3.103$, and $a(\text{MOVPE-AlN}) = 3.106$ Å. The AlN c-lattice constants were $c(\text{DGA-AlN}) = 4.987$, $c(\text{AlN:Si/DGA-AlN}) = 4.990$, and $c(\text{MOVPE-AlN}) = 4.992$ Å.

The different AlN templates were overgrown simultaneously in the same growth run to ensure that the LED heterostructures are identical. The LED heterostructures consist of a 500 nm AlN buffer, an 875 nm thick n-Al_{0.85}Ga_{0.15}N:Si contact layer grown at 1080 °C and 200 hPa, and a threefold Al_{0.76}Ga_{0.24}N MQW embedded in 35 nm thick lower, 5 nm thick inner, and 20 nm thick upper Al_{0.8}Ga_{0.2}N barriers. On top of the MQW active region, an 80 nm thick, non-intentionally doped (nid), compositionally graded AlGaIn layer with a grading from AlN to Al_{0.76}Ga_{0.24}N was grown (all at 1030 °C and 400 hPa) and capped by 30 nm p⁺⁺-GaIn:Mg. The layer thicknesses and curvature of the wafers were determined from *in situ* reflectivity data at 405 nm. The thicknesses were additionally checked by scanning electron microscopy on cross sections of LED heterostructures.

Flip chip mountable, bottom emitting LEDs were fabricated using standard chip-processing technologies. Mesa structures with 0.4 mm² emitting active area were defined by inductively coupled plasma etching in order to expose the n-AlGaIn contact layer. Platinum-based p-contacts and vanadium-aluminum based n-contacts³⁴ were deposited to form the p-electrode and the n-electrode, respectively. The electrical and optical characteristics of the LEDs were measured on-wafer under cw operation at room temperature. For that purpose, the wafers were placed epi-side up on a sample holder without any active cooling. The emission spectra and the optical power and operation voltage vs current (L-I-V) characteristics were measured by collecting the light emitted through the substrate with an optical fiber spectrometer and a calibrated silicon photodiode, respectively. Selected LEDs were diced and flip-chip mounted on AlN ceramic packages. These packaged LEDs were measured at a constant temperature of 20 °C under cw operation in a calibrated integrating sphere.

The DOP of the emission from the LEDs was determined by analyzing the in-plane emission from cleaved facets by a polarization-dependent electro-luminescence (EL) setup using a Glan-Taylor prism.^{11,14}

Figure 1 shows the curvature (K) of the three different wafers during MOVPE growth of the far-UVC LED heterostructure. The *in situ* measurements reveal that after heating up, the initial 500 nm AlN layer on the MOVPE-AlN template (light gray graph) grows under tensile strain with a positive $\Delta K/\Delta t$ of +0.006 km⁻¹/s. This is commonly observed during the growth of thicker AlN as long as dislocation annihilation takes place, and no relaxation by cracking or formation of new dislocations occurs.³⁴ In contrast, the AlN layer on the DGA-AlN template grows under strong compressive strain with a negative slope of the curvature of -0.015 km⁻¹/s (black graph). For the AlN growth on the AlN:Si/DGA-AlN template, the slope of curvature is zero (gray graph), demonstrating the successful compensation of the compressive strain by growth of Si-doped AlN.

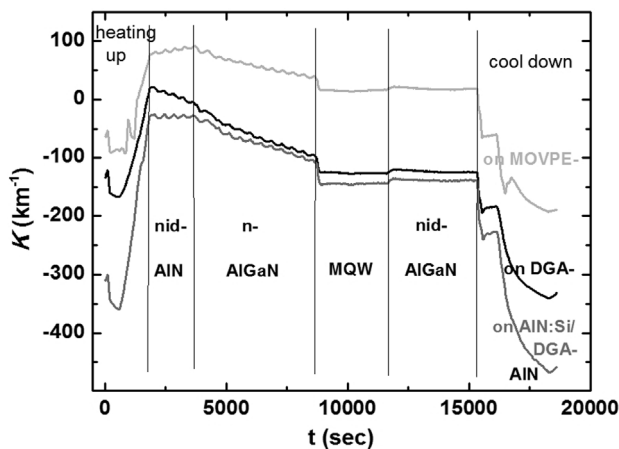


FIG. 1. *In situ* curvature K transients during MOVPE growth of the far UVC-LED heterostructure on non-annealed MOVPE-AIN- (light gray), AlN:Si/DGA-AIN- (gray), and DGA-AIN (black) templates.

The *in situ* curvature measurements during AlN growth clearly show that the three different AlN templates offer different a-lattice constants and, hence, introduce different strain states into the subsequently grown LED heterostructure.

The subsequently grown $n\text{-Al}_{0.85}\text{Ga}_{0.15}\text{N:Si}$ current spreading layer grows compressively on all three templates. The smallest slope $\Delta K/\Delta t$ of $-0.009\text{ km}^{-1}/\text{s}$ is observed for the layer deposited on the MOVPE-AIN template. The biggest slope $\Delta K/\Delta t$ of $-0.016\text{ km}^{-1}/\text{s}$ is seen for the layers on the DGA-based templates (DGA-AIN and AlN:Si/DGA-AIN). The linear behavior of the curvature suggests that no additional relaxation occurs during the growth of the $n\text{-Al}_{0.85}\text{Ga}_{0.15}\text{N:Si}$ layer. On the MOVPE-AIN template with a TDD of around $2 \times 10^9\text{ cm}^{-2}$, the main relaxation mechanism is the inclination of the threading dislocations starting at the interface between AlN and $n\text{-Al}_{0.85}\text{Ga}_{0.15}\text{N}$.^{32,34–36} Due to the low dislocation density in the DGA-based AlN templates, the relaxation of compressive strain mediated by preexisting dislocations is limited. Annular dark field scanning

transmission electron microscopy of cross sections of such heterostructures on DGA-based templates³² revealed that relaxation takes place by dislocation bending and formation of dislocation half-loops of irregular shape, which accumulate at the homoepitaxial MOVPE-AIN/DGA-AIN interface. The slopes of the curvature during the growth of the MQW region are zero within measurement accuracy, especially considering the extremely low growth rates and layer thicknesses. The relaxation degrees of the $n\text{-Al}_{0.85}\text{Ga}_{0.15}\text{N}$ and $\text{Al}_{0.81}\text{Ga}_{0.19}\text{N}$ barriers determined from reciprocal space maps (RSMs) were 26%, 22%, and 5% grown on the MOVPE-AIN, AlN:Si/DGA-AIN, and DGA-AIN templates, respectively. The CL dark spot densities (monochromatic at the MQW emission wavelength) for samples grown under the same growth conditions as the full LED heterostructures but terminated after the MQW active region were 1.5×10^9 and $6 \times 10^8\text{ cm}^{-2}$ for MOVPE-AIN and for the DGA-based structures, respectively. This suggests that no significant relaxation via dislocation formation took place during AlGaIn growth.

Figure 2 shows typical electroluminescence spectra of the LEDs grown on different AlN templates for bottom emission through the substrate [Fig. 2(a)] and in-plane emission from cleaved facets [Fig. 2(b)]. The peak emission wavelength of the LEDs across the wafers was 232–237 nm, 231–235 nm, and 229–233 nm for the LEDs grown on MOVPE-, AlN:Si/DGA-, and DGA-AIN templates, respectively. The observed shorter wavelength (1–3 nm) for the LEDs with higher compressive strain (lower relaxation) can be attributed to the higher valence band separation expected from simulations by the $\mathbf{k}\cdot\mathbf{p}$ theory.¹⁷ The spectra of the LEDs based on MOVPE-AIN templates consist of a single emission peak without significant parasitic luminescence. The spectra of both DGA-based LEDs show additional parasitic luminescence peaks at longer wavelengths around 370 nm (between 300 and 450 nm) [Fig. 2(a)]. These peaks are caused by DGA-AIN and the underlying sapphire as identified by cathodoluminescence from cross sections of the DGA-based templates. Kai *et al.* found that the intensity of these peaks correlates with the temperature and duration of the annealing.³⁷ It was assumed that the increased oxygen concentration in AlN during high temperature annealing causes the formation of point defects ($[\text{V}_{\text{Al}}-\text{n}(\text{O}_{\text{N}})]$, V_{N}) and, therefore, enhances near ultraviolet emission. The QW-emission is absorbed by the defect

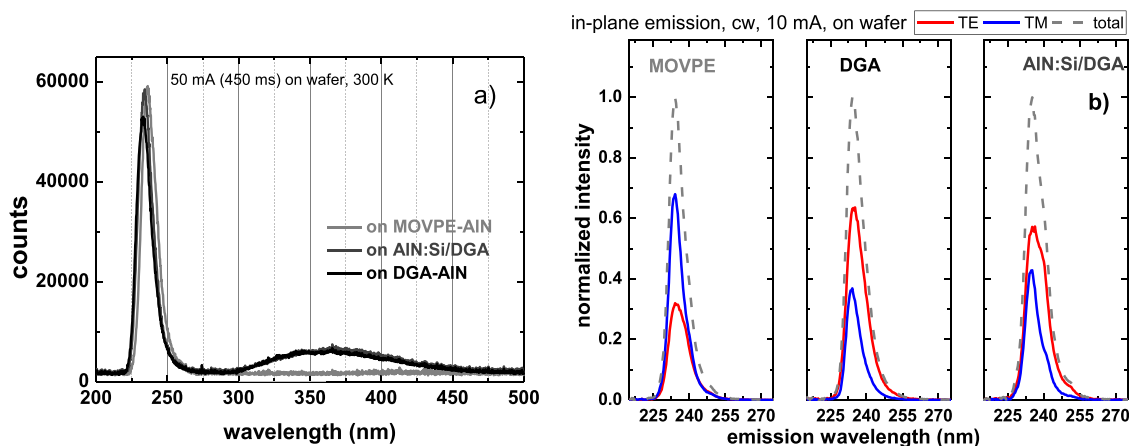


FIG. 2. Typical electroluminescence spectra of LEDs measured on-wafer from the backside of MOVPE- (a, gray), AlN:Si/DGA- (a, dark gray), and DGA-AIN/sapphire templates (a, black) as well as in-plane spectra of LEDs measured from the mesa edge (b) for different polarizations.

complexes in DGA-AlN and defect luminescence is excited as we will show in more detail in a separate publication.

The typical EL spectra of the in-plane emission of the LEDs grown on the different AlN templates reveal the shift from dominant TM polarized emission for the LEDs on the MOVPE-AlN template to more TE polarized emission on the DGA-based template [Fig. 2(b)]. This trend agrees well with the band structure calculations for the different strained heterostructures.^{11,17} The observed small shoulder on the long wavelength side of the QW-emission from LEDs on the AlN:Si/DGA-AlN template can be correlated with a slight gallium enrichment in the QWs at macro-steps formed during the deposition of the very thick AlN:Si layer.

Figure 3 shows the measured DOP = $(I_{TE} - I_{TM}) / (I_{TE} + I_{TM})$ of the integrated intensities, I_{TE} and I_{TM} , of the in-plane EL spectra for TE and TM polarized light, respectively, for LEDs grown on the different AlN templates vs the a - and c -lattice constants of different AlN templates determined from the RSMs. The lowest DOP of -0.23 ± 0.03 was observed for the LED structure grown on the non-annealed MOVPE-AlN template. As expected for emission wavelengths below 240 nm, TM polarized emission is dominant. The in-plane a -lattice parameter of this AlN template is the largest with 3.106 Å. For the LEDs on DGA-AlN, the DOP is 0.37 ± 0.03 , i.e., the TE polarized emission is dominating. The in-plane a -lattice parameter of the DGA-AlN template is the smallest with 3.100 Å. This explains the strong compressive strain during growth of the non-intentionally doped AlN buffer layer seen in Fig. 1. Although annealing at 1720 °C led to a bigger lattice constant in comparison to the MOVPE-grown AlN with deposition temperatures around 1110 °C, the stronger lattice contraction of the sapphire during the cooldown leads to a compressively strained layer with a smaller a - and a bigger c -lattice constant.

For the LEDs on the AlN:Si/DGA-AlN template, the measured DOP is 0.25 ± 0.04 , i.e., the emission is also dominated by TE polarized light. The a -lattice parameter of the template (3.103 Å) is between the values of the DGA- and MOVPE-AlN templates. The smaller DOP of the LEDs on the AlN:Si/DGA template in comparison to the DGA template is attributed to the higher degree of relaxation, determined by the RSMs and supported by the longer emission wavelength as predicted by the band structure calculations.

The significant differences in DOP of the LEDs on different AlN templates should have a significant influence on the LEE.¹¹ Since it is known that the IQE is strongly reduced with shorter wavelength, only LEDs with the same emission wavelength of 232–233 nm were used for a fair comparison of the LEE. The mean values of on-wafer emission power at 50 mA (cw) were 0.28 ± 0.1 , 0.44 ± 0.26 , and 0.73 ± 0.17 mW on MOVPE-, AlN:Si/DGA-, and DGA-AlN templates, respectively. The DGA based structures have the same dislocation density acting as non-radiative recombination centers. Thus, the difference in optical output power (nearly 1.7-fold higher output for the mean value or ~ 1.3 -fold for the maximum values) can be attributed to the different strain induced by the template. The LEE was calculated based on the measured DOPs and assuming a similar IQE of the MQWs of the LED structures grown on the DGA-based AlN templates.¹⁶ The measured increase in the DOP from 0.25 to 0.37 leads to an increase in the outcoupling efficiency from 2.65% to 2.79%, i.e., by only a factor of about 1.05 from AlN:Si/DGA to the DGA template, much less than the measured increase in output power. This means that the IQE cannot be the same for the LEDs grown on the two types of DGA-based AlN templates. Considering the wavelength shift by the introduced strain for the same Al content of the QWs maybe the comparison of the emission power should be done not at exactly the same wavelength, but for the shifted emission wavelengths of the LEDs based on the different DGA templates, i.e., at 232 and 231 nm.

For the LEDs on the MOVPE template, two factors limit the output power—first, the low LEE due to the dominant TM polarization and, second, the higher density of dislocations acting as non-radiative centers reducing the IQE. The introduction of the annealing steps of the AlN/sapphire templates led to an increase in the output power by a factor of 1.6 (AlN:Si/DGA template) and 2.6 (DGA template), respectively. For the AlN:Si/DGA-AlN template, the strain relaxation is nearly the same as for the MOVPE-AlN template. Simulating the LEE for these structures based on their DOP the output power should increase by a factor of about 1.3, which is slightly below the measured value of 1.6 (1.4 for maximum values). This can be attributed to the different TDDs of the MQWs in the LED heterostructures deposited on the MOVPE-AlN template ($15 \times 10^8 \text{ cm}^{-2}$) and on the AlN:Si/DGA template ($6 \times 10^8 \text{ cm}^{-2}$). It seems that for the LEDs on annealed

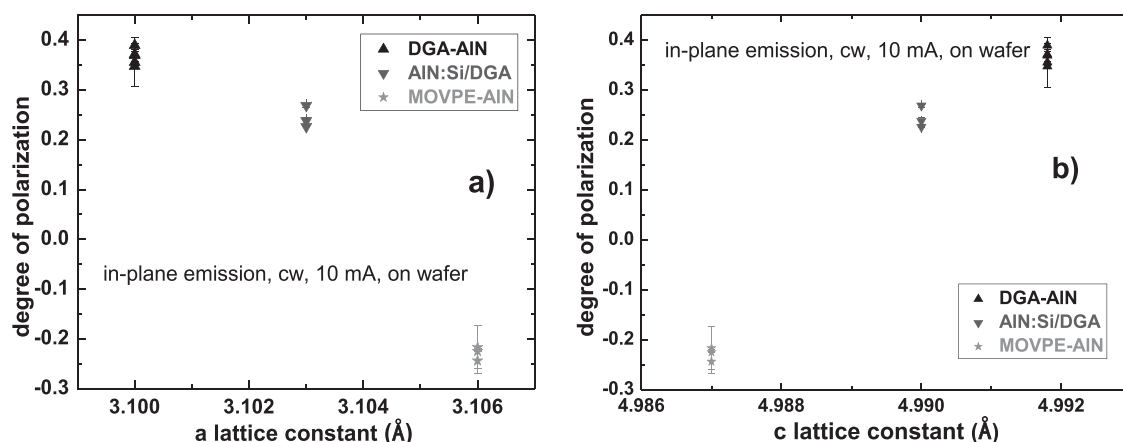


FIG. 3. Degree of polarization of emission from LEDs based on different AlN templates and in-plane a - [Fig. 3(a)] and perpendicular c - [Fig. 3(b)] lattice parameters of the AlN templates. Gray, dark gray, and black symbols for LEDs on MOVPE-, AlN:Si/DGA-, and DGA-AlN templates, respectively.

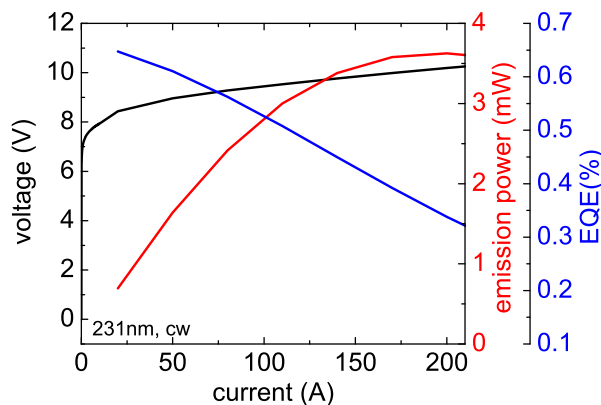


FIG. 4. Optical output-power, current–voltage characteristics, and external quantum efficiency of flip-chip mounted far-UVC LEDs on the DGA-AlN template measured in an integrating sphere under cw operation at 20 °C.

templates, the difference in TDD has less influence on the optical output power than the different strain states. This may be related to the relatively small radius for capture of carriers into dislocations in AlGaIn with high Al content as observed in Ref. 38.

Figure 4 shows the L–I–V characteristic of a flip-chip mounted far-UVC LED on a DGA-AlN template measured in an integrating sphere under cw operation at 20 °C. The LED emitting at 231 nm reaches an optical output power of 3.5 mW at 150 mA (2.8 mW at 100 mA). Its external quantum efficiency (EQE) and wall plug efficiency at 20 mA were 0.65% and 0.42%, respectively. This reveals the positive effect of the introduced compressive strain and lower dislocation density by the use of DGA-AlN/sapphire templates for fabrication of far-UVC LED structures.

We have demonstrated that strain management and defect reduction in DGA-AlN/sapphire templates having undergone two annealing steps can significantly improve the performance of far-UVC LEDs. Due to the additional compressive strain resulting from the smaller in-plane AlN lattice constant of DGA-AlN/sapphire templates, the crossover point from TE to TM polarized emission can be shifted from 245 to near 230 nm yielding an improved LEE at short wavelengths. Based on these advances, flip-chip mounted far-UVC LEDs emitting at 231 nm with optical output power of more than 3.5 mW under cw operation have been demonstrated. In the near future, a combination of high temperature annealed AlN and structured sapphire substrates could even further increase the LEE and output power of far-UVC-LEDs.

The authors would like to thank C. Neumann and T. Petzke for their technical help in the operation of the MOVPE reactors as well as C. Netzel and H. Lawrenz for cathodoluminescence and A. Mogilatenko for transmission electron microscopy investigations. This work was supported by the German Federal Ministry of Education and Research (BMBF) under Contract No. 03COV10E.

AUTHOR DECLARATIONS

Conflict of Interest

The authors have no conflicts to disclose.

Author Contributions

Arne Knauer: Investigation (lead); Writing – original draft (lead). **Michael Kneissl:** Funding acquisition (equal); Project administration (equal); Writing – review & editing (equal). **Markus Weyers:** Funding acquisition (equal); Project administration (equal); Supervision (equal); Writing – review & editing (equal). **Tim Kolbe:** Data curation (equal); Investigation (equal). **Sylvia Hagedorn:** Data curation (equal); Investigation (equal); Writing – review & editing (equal). **Jakob Höpfner:** Data curation (equal); Investigation (equal). **Martin Guttman:** Data curation (equal); Writing – review & editing (equal). **Hyun Kyong Cho:** Investigation (equal). **Jens Rass:** Investigation (equal); Writing – review & editing (equal). **Jan Ruschel:** Data curation (equal); Investigation (equal). **Sven Einfeldt:** Project administration (equal); Writing – review & editing (equal).

DATA AVAILABILITY

The data that support the findings of this study are available from the corresponding author upon reasonable request.

REFERENCES

- Glaab, N. Lobo-Ploch, H. K. Cho, T. Filler, H. Gundlach, M. Guttman, S. Hagedorn, S. B. Lohan, F. Mehnke, J. Schleusener, C. Sicher, L. Sulmoni, T. Wernicke, L. Wittenbecher, U. Woggon, P. Zwicker, A. Kramer, M. C. Meinke, M. Kneissl, M. Weyers, U. Winterwerber, and S. Einfeldt, *Sci. Rep.* **11**, 14647 (2021).
- M. Buonanno, B. Ponnaiya, D. Welch, M. Stanislauskas, G. Randers-Pehrson, L. Smilenov, F. D. Lowy, D. M. Owens, and D. J. Brenner, *Radiat. Res.* **187**, 483 (2017).
- M. Buonanno, G. Randers-Pehrson, A. W. Bigelow, S. Trivedi, F. D. Lowy, H. M. Spotnitz, S. M. Hammer, and D. J. Brenner, *PLoS One* **8**, e76968 (2013).
- K. Narita, K. Asano, K. Naito, H. Ohashi, M. Sasaki, Y. Morimoto, T. Igarashi, and A. Nakane, *J. Hosp. Infect.* **105**(3), 459 (2020).
- H. Shimoda, J. Matsuda, T. Iwasaki, and D. Hayasaka, *J. Photochem. Photobiol.* **7**, 100050 (2021).
- P. Zwicker, J. Schleusener, S. B. Lohan, L. Busch, C. Sicher, S. Einfeldt, M. Kneissl, A. A. Kühn, C. M. Keck, C. Witzel, A. Kramer, and M. C. Meinke, *Sci. Rep.* **12**, 2587 (2022).
- T. Fukui, T. Niihara, T. Oda, Y. Kumabe, H. Ohashi, M. Sasaki, T. Igarashi, M. Kunisada, N. Yamano, K. Oe, T. Matsumoto, T. Matsushita, S. Hayashi, C. Nishigori, and R. Kuroda, *PLoS One* **15**(8), e0235948 (2020).
- Y. Taniyasu, M. Kasu, and T. Makimoto, *Nature* **441**, 325 (2006).
- M. Kneissl, T.-Y. Seong, J. Han, and H. Amano, *Nat. Photonics* **13**, 233 (2019).
- A. Yoshikawa, R. Hasegawa, T. Morishita, K. Nagase, S. Yamada, J. Grandusky, J. Mann, A. Miller, and L. J. Schowalter, *Appl. Phys. Express* **13**(2), 022001 (2020).
- C. Reich, M. Guttman, M. Feneberg, T. Wernicke, F. Mehnke, C. Kuhn, J. Rass, M. Lapeyrate, S. Einfeldt, A. Knauer, V. Kueller, M. Weyers, R. Goldhahn, and M. Kneissl, *Appl. Phys. Lett.* **107**(14), 142101 (2015).
- R. G. Banal, M. Funato, and Y. Kawakami, *Phys. Rev. B* **79**(12), 121308 (2009).
- S.-H. Park and J.-I. Shim, *Appl. Phys. Lett.* **102**, 221109 (2013).
- T. Kolbe, A. Knauer, C. Chua, Z. Yang, S. Einfeldt, P. Vogt, N. M. Johnson, M. Weyers, and M. Kneissl, *Appl. Phys. Lett.* **97**, 171105 (2010).
- M. Guttman, J. Hoepfner, C. Reich, L. Sulmoni, C. Kuhn, P. Roeder, T. Wernicke, and M. Kneissl, *Semicond. Sci. Technol.* **34**, 085007 (2019).
- M. Guttman, F. Mehnke, B. Belde, F. Wolf, C. Reich, L. Sulmoni, T. Wernicke, and M. Kneissl, *Jpn. J. Appl. Phys.* **58**, SCCB20 (2019).
- Z. Bryan, I. Bryan, S. Mita, J. Tweedie, Z. Sitar, and R. Collazo, *Appl. Phys. Lett.* **106**, 232101 (2015).
- H. Long, S. Wang, J. Dai, F. Wu, J. Zhang, J. Chen, R. Liang, Z. C. Feng, and C. Cheng, *Opt. Express* **26**(2), 680 (2018).
- A. Szein, J. E. Bowers, S. P. Denbaars, and S. Nakamura, *Appl. Phys. Lett.* **104**, 042106 (2014).

- ²⁰F. Bernardini, V. Fiorentini, and D. Vanderbilt, *Phys. Rev. B* **56**, R10024 (1997).
- ²¹H. Hirayama, N. Noguchi, T. Yatabe, and N. Kamata, *Appl. Phys. Express* **1**, 051101 (2008).
- ²²M. Jo, Y. Itokazu, and H. Hirayama, *Appl. Phys. Lett.* **120**, 211105 (2022).
- ²³D. Liu, S. J. Cho, J. Park, J. H. Seo, R. Dalmau, D. Zhao, K. Kim, J. Gong, M. Kim, I. K. Lee, J. D. Albrecht, W. Zhou, B. Moody, and Z. Ma, *Appl. Phys. Lett.* **112**, 081101 (2018).
- ²⁴N. Lobo-Ploch, F. Mehnke, L. Sulmoni, H. K. Cho, M. Guttman, J. Glaab, K. Hilbrich, T. Wernicke, S. Einfeldt, and M. Kneissl, *Appl. Phys. Lett.* **117**, 111102 (2020).
- ²⁵D. Wang, K. Uesugi, S. Xiao, K. Norimatsu, and H. Miyake, *Appl. Phys. Express* **13**, 095501 (2020).
- ²⁶H. Miyake, C. H. Lin, K. Tokoro, and K. Hiramatsu, *J. Cryst. Growth* **456**, 155 (2016).
- ²⁷S. Hagedorn, S. Walde, A. Knauer, N. Susilo, D. Pacak, L. Cancellara, C. Netzel, A. Mogilatenko, C. Hartmann, T. Wernicke, M. Kneissl, and M. Weyers, *Phys. Status Solidi (a)* **217**(14), 1901022 (2020).
- ²⁸T. Metzger, R. Höpler, E. Born, O. Ambacher, M. Stutzmann, R. Stömmer, M. Schuster, H. Göbel, S. Christiansen, M. Albrecht, and H. P. Strunk, *Philos. Mag. A* **77**(4), 1013 (1998).
- ²⁹M. X. Wang, F. J. Xu, N. Xie, Y. H. Sun, B. Y. Liu, W. K. Ge, X. N. Kang, Z. X. Qin, X. L. Yang, X. Q. Wang, and B. Shen, *Appl. Phys. Lett.* **114**, 112105 (2019).
- ³⁰C.-Y. Huang, S. Walde, C.-L. Tsai, C. Netzel, H.-H. Liu, S. Hagedorn, Y.-R. Wu, Y.-K. Fu, and M. Weyers, *Jpn. J. Appl. Phys.* **59**, 070904 (2020).
- ³¹S. Walde, C.-Y. Huang, C.-L. Tsai, W.-H. Hsieh, Y.-K. Fu, S. Hagedorn, H.-W. Yen, T.-C. Lu, M. Weyers, and C.-Y. Huang, *Acta Mater.* **226**, 117625 (2022).
- ³²A. Mogilatenko, S. Walde, S. Hagedorn, C. Netzel, C.-Y. Huang, and M. Weyers, *J. Appl. Phys.* **131**, 045702 (2022).
- ³³J. Weinrich, A. Mogilatenko, F. Brunner, C. T. Koch, and M. Weyers, *Appl. Phys. Lett.* **126**, 085701 (2019).
- ³⁴A. Knauer, A. Mogilatenko, J. Weinrich, S. Hagedorn, S. Walde, T. Kolbe, L. Cancellara, and M. Weyers, *Cryst. Res. Technol.* **55**, 1900215 (2020).
- ³⁵A. E. Romanov and J. S. Speck, *Appl. Phys. Lett.* **83**, 2569 (2003).
- ³⁶Z. Wu, K. Nonaka, Y. Kawai, T. Asai, F. A. Ponce, C. Chen, M. Iwaya, S. Kamiyama, H. Amano, and I. Akasaki, *Appl. Phys. Express* **3**, 111003 (2010).
- ³⁷C. Kai, H. Zang, J. Ben, K. Jiang, Z. Shi, Y. Jia, X. Cao, W. Lü, X. Sun, and D. Li, *J. Luminescence* **235**, 118032 (2021).
- ³⁸C. Netzel, A. Knauer, F. Brunner, A. Mogilatenko, and M. Weyers, *Phys. Status Solidi (b)* **258**(11), 2100358 (2021).